

Resonant inelastic x-ray scattering in layered trimer iridate $\text{Ba}_4\text{Ir}_3\text{O}_{10}$: the density functional approach

D.A. Kukusta,¹ L.V. Bekenov,¹ and V.N. Antonov^{1,2}

¹*G. V. Kurdyumov Institute for Metal Physics of the N.A.S. of Ukraine,
36 Academician Vernadsky Boulevard, UA-03142 Kyiv, Ukraine*

²*Max-Planck-Institute for Solid State Research, Heisenbergstrasse 1, 70569 Stuttgart, Germany*

(Dated: February 18, 2026)

We have investigated the electronic structure of $\text{Ba}_4\text{Ir}_3\text{O}_{10}$ within the density-functional theory (DFT) using the generalized gradient approximation while considering strong Coulomb correlations (GGA+U) in the framework of the fully relativistic spin-polarized Dirac linear muffin-tin orbital band-structure method. $\text{Ba}_4\text{Ir}_3\text{O}_{10}$ has a quasi-2D structure composed of buckled sheets, which constitute corner-connected Ir_3O_{12} trimers containing three distorted face-sharing IrO_6 octahedra. The Ir atoms are distributed over two symmetrically inequivalent sites: the center of the trimer (Ir_1) and its two tips (Ir_2). The $\text{Ir}_1 - \text{Ir}_2$ distance within the trimer is quite small and equals to 2.58 Å at low temperature. As a result, the clear formation of bonding and antibonding states at the Ir_1 site occurs. The large bonding-antibonding splitting stabilizes the d_{yz} -orbital-dominant antibonding state of t_{2g} holes and produces a wide energy gap at the Fermi level. However, the energy gap opens up only with taking into account strong Coulomb correlations at the Ir_2 site. Therefore, we have quite a unique situation when the insulating state is driven by both the dimerization at the Ir_1 site and Mott insulating behavior at the Ir_2 one. We have investigated resonant inelastic x-ray scattering (RIXS) spectra at the Ir L_3 edge. The calculated results are in good agreement with experimental data. The RIXS spectrum possesses several sharp features below 2.1 eV corresponding to transitions within the Ir t_{2g} levels. The excitation located from 2.1 to 4.6 eV is due to $t_{2g} \rightarrow e_g$ and $\text{O}_{2p} \rightarrow t_{2g}$ transitions. The wide structure situated at 6.2–12 eV appears due to charge transfer and $\text{O}_{2p} \rightarrow e_g$ transitions. We have also presented comprehensive theoretical calculations of the RIXS spectrum at the oxygen K edge.

PACS numbers: 75.50.Cc, 71.20.Lp, 71.15.Rf

I. INTRODUCTION

Interplay between orbital, spin, charge carriers, and lattice degrees of freedom has been a fascinating subject for the condensed-matter physics community for the last few decades. The 5d transition-metal compounds possess the same order of magnitude of on-site Coulomb repulsion U , spin-orbit coupling (SOC), and the crystal-field energy [1]. SOC in such systems splits the t_{2g} orbitals into a quartet ($J_{\text{eff}} = \frac{3}{2}$) and a doublet ($J_{\text{eff}} = \frac{1}{2}$) [1–3]. In $5d^5$ (Ir^{4+}) iridium oxides, such as Sr_2IrO_4 , the quartet $J_{\text{eff}} = \frac{3}{2}$ is fully occupied, and the relatively narrow $J_{\text{eff}} = \frac{1}{2}$ doublet, occupied by one electron, can be splitted by moderate Hubbard U_{eff} with opening a small band gap called the relativistic Mott gap [4–7]. Iridates have been at the center of intensive research in recent years for novel phenomena, such as topological insulators [8–11], Mott insulators [4, 5, 12, 13], Weyl semimetals [14–16], and quantum spin liquids (QSLs) [17–19].

The specific physical properties of iridates strongly depend on local geometry. The cases most widely discussed in the literature are the geometry with MO_6 octahedra (M is a transition-metal ion) sharing a common oxygen (a common corner) or two common oxygens (octahedra with a common edge). The first case takes place, for example, in the LaMnO_3 perovskite or layered systems as La_2CuO_4 . The case with a common edge occurs in many layered systems with triangular lattices such as NaCoO_2

and LiNiO_2 . The features of spin-orbit systems in both these cases were studied in detail (see, e.g., Ref. [20]). The third typical geometry, which can also be very often met in many real materials, is the case of octahedra with a common face (three common oxygens). Actually, there are many transition-metal compounds with this geometry [21]. Such materials include, for example, the series of perovskites $\text{Ba}_3\text{MIr}_2\text{O}_9$ (M = Y^{3+} , Sc^{3+} , In^{3+} , Lu^{3+}) [22, 23], which show diverse ground-state properties. These systems possess blocks of two face-sharing IrO_6 octahedra separated by MO_6 octahedra (which have common corners with IrO_6). They have two equivalent Ir sites, therefore, the oxidation state of Ir in these systems is fractional: $\text{Ba}_3\text{M}^{3+}\text{Ir}_2^{4,5+}\text{O}_9$. This fractional oxidation state of Ir (accompanied by a unique crystallographic site) can lead to fascinating ground states. At high temperatures, where the mixed-valence Ir_2O_9 dimers can be seen as isolated, the magnetic susceptibility deviates from the conventional Curie-Weiss behavior [22, 24, 25] suggesting nontrivial temperature evolution of the local magnetic moment. At low temperatures, interactions between the dimers become important, and signatures of frustrated magnetic behavior [26] including possible formation of a spin-liquid ground state have been reported [27].

Another example with two blocks of face-sharing octahedra is the $\text{Ba}_5\text{AlIr}_2\text{O}_{11}$ barium oxide. The crystal structure of this compound consists of AlO_4 tetrahedra and IrO_6 octahedra. The latter octahedra share a face

and develop Ir_2O_9 dimers. Novel properties are expected from this structural arrangement in addition to those driven by SOC. Opposite to the $\text{Ba}_3\text{M}\text{Ir}_2\text{O}_9$ systems, $\text{Ba}_5\text{Al}\text{Ir}_2\text{O}_{11}$ features dimer chains of two inequivalent octahedra occupied by tetravalent Ir^{4+} ($5d^5$) and pentavalent Ir^{5+} ($5d^4$) ions, respectively. $\text{Ba}_5\text{Al}\text{Ir}_2\text{O}_{11}$ is a Mott insulator that undergoes a subtle structural phase transition near $T_S = 210$ K and a transition to magnetic order at $T_M = 4.5$ K. The ferrimagnetic (FiM) state below T_M is highly anisotropic and resilient to a strong magnetic field (up to 14 T) but is susceptible to even modest hydrostatic pressure [28].

Recently, unconventional electronic and magnetic ground states have been reported in compounds with basic units of Ir trimers, i.e., three face-sharing IrO_6 octahedra, which are much less explored so far [29–31]. Among them, $\text{Ba}_4\text{Ir}_3\text{O}_{10}$ with a Ir $5d^5$ nominal atomic configuration and a monoclinic $P2_1/a$ structure [32]. It has a quasi-2D structure composed of buckled sheets, which constitute corner-connected Ir_3O_{12} trimers containing three distorted face-sharing IrO_6 octahedra. The Ir atoms are distributed over two symmetrically inequivalent sites: Ir_1 , at the center of the trimers, is at the Wyckoff position $2a$, and two outer Ir_2 atoms are at the Wyckoff position $4e$. The shortest Ir-Ir bond is the one between Ir_1 and Ir_2 within the trimers, which has a length of ~ 2.58 Å [31, 33], shorter than in the metallic iridium (~ 2.71 Å [34]) and in the dimer perovskites $\text{Ba}_3\text{In}\text{Ir}_2\text{O}_9$ (~ 2.65 Å [27]) and $\text{Ba}_5\text{Al}\text{Ir}_2\text{O}_{11}$ (~ 2.73 Å [35]).

Here we report a theoretical investigation of the electronic and magnetic structures of the $\text{Ba}_4\text{Ir}_3\text{O}_{10}$ perovskite. There are several experimental investigations of its physical properties with some controversial results and conclusions [21, 31, 32, 36–40]. The transport and magnetization studies by Cao *et al.* [31] found no magnetic order down to 0.2 K despite the Curie-Weiss temperatures up to -766 K and an enormously large averaged frustration parameter ($f \sim 2000$). In contrast, the material shows linear behavior in the low-temperature magnetic heat capacity, resembling a gapless quantum spin liquid (QSL). In fact, the ground state is rather fragile in regard to external perturbations including sample growth conditions [32, 39] and chemical doping: even a slight substitution of 1 or 2% isovalent Sr for Ba recovers the magnetic order and destroys the signatures of the QLS [31]. Together, these reports suggest that the magnetic ground state properties of $\text{Ba}_4\text{Ir}_3\text{O}_{10}$ are extremely delicate. Although Gao *et al.* [31] has speculated that $\text{Ba}_4\text{Ir}_3\text{O}_{10}$ could be either a Luttinger liquid QSL or a 2D QSL such as spinon Fermi surface states, the authors of Ref. [40] argue that $\text{Ba}_4\text{Ir}_3\text{O}_{10}$ possesses a 1D spinon continuum. Therefore, instead of forming an isotropic QSL state, the magnetic frustration can effectively reduce the system dimension, suppressing the magnetic order and realizing deconfined spinons in a unique way.

Cao *et al.* [39] investigated the physical properties of structurally altering $\text{Ba}_4\text{Ir}_3\text{O}_{10}$ via application of a magnetic field during materials growth. The magnetic field

itself was remarkably very weak, no stronger than 0.06 Tesla. Structurally, the field-altered single crystal exhibits an elongation in the b axis with only slight changes in the a and c axes as well as the increase of both Ir-Ir bond distances within each trimer and the Ir-O-Ir bond angle between the trimers. They found that small changes in the lattice constants and bond angles cause disproportionately large electronic changes. The quantum liquid in the non-altered $\text{Ba}_4\text{Ir}_3\text{O}_{10}$ is replaced with the AFM state in the field-altered $\text{Ba}_4\text{Ir}_3\text{O}_{10}$, emphasizing the critical role of SOI and Coulomb correlations in this class of quantum materials.

Recently, Chen *et al.* [32] utilized together resonant elastic x-ray scattering (REXS), magnetometry, and specific heat to investigate the ground state properties of $\text{Ba}_4\text{Ir}_3\text{O}_{10}$ single crystals. In contrast to previous results [31], the authors discovered clear magnetic order in $\text{Ba}_4\text{Ir}_3\text{O}_{10}$. The scattering data revealed two consecutive second order structural and magnetic transitions at $T_S \sim 142$ K and $T_N \sim 25$ K, respectively. The two transitions are consistent with the kinks in the anisotropic magnetization data, which are qualitatively similar to the data from the previous report [31]. Shen *et al.* [40] by measuring the RIXS spectra at the Ir L_3 edge found clear evidence of magnon excitations at low energy (~ 0.1 eV) in $\text{Ba}_4\text{Ir}_3\text{O}_{10}$, and therefore, this oxide couldn't be characterized as QSL.

In this paper, we focus our attention on the RIXS properties of $\text{Ba}_4\text{Ir}_3\text{O}_{10}$. The RIXS method has shown remarkable progress as a spectroscopic technique to record the momentum and energy dependence of inelastically scattered photons in complex materials. RIXS rapidly became the forefront of experimental photon science [41, 42]. It combines spectroscopy and inelastic scattering to probe the electronic structure of materials. This method is bulk sensitive, polarization dependent, as well as element and orbital specific [41]. It permits direct measurements of phonons, plasmons, single-magnons, and orbitons, as well as other many-body excitations in strongly correlated systems, such as cuprates, nickelates, osmates, ruthenates, and iridates, with complex low-energy physics and exotic phenomena in the energy and momentum space.

There is great progress in the RIXS experiments over the past decade. The most calculations of the RIXS spectra of various materials have been carried out using the atomic multiplet approach with some adjustable parameters and the number of theoretical first-principle calculations of RIXS spectra is extremely limited. In this paper, we report a theoretical investigation from the first principles of the RIXS spectra of $\text{Ba}_4\text{Ir}_3\text{O}_{10}$. Recently, the RIXS measurements have been successfully performed at the Ir L_3 edge in $\text{Ba}_4\text{Ir}_3\text{O}_{10}$ by Shen *et al.* [40] in the energy range up to 5 eV. In addition to the elastic peak centered at zero energy loss, the spectrum consists of several peaks below 2 eV and a peak at 3.8 eV. The authors also discovered low-energy magnetic excitations at ~ 0.1 eV. They also presented the RIXS spectra at the Ir L_3

edge of the isovalently doped $(\text{Ba}_{1-x}\text{Sr}_x)_4\text{Ir}_3\text{O}_{10}$ ($x = 0.02$).

We carry out here a detailed study of the electronic structure and RIXS spectra of $\text{Ba}_4\text{Ir}_3\text{O}_{10}$ in terms of the density functional theory. Our study sheds light on the important role of band structure effects and transition metal $5d$ – oxygen $2p$ hybridization in the spectral properties of $5d$ oxides. We use the *ab initio* approach using the fully relativistic spin-polarized Dirac linear muffin-tin orbital band-structure method. Both the generalized gradient approximation (GGA) and the GGA+ U approach are used to assess the sensitivity of the RIXS results to different treatment of the correlated electrons.

The paper is organized as follows. The crystal structure of $\text{Ba}_4\text{Ir}_3\text{O}_{10}$ and computational details are presented in Sec. II. Section III presents the electronic and magnetic structures of $\text{Ba}_4\text{Ir}_3\text{O}_{10}$. In Sec. IV, the theoretical investigation of the RIXS spectrum of $\text{Ba}_4\text{Ir}_3\text{O}_{10}$ at the Ir L_3 and oxygen K edges is presented, the theoretical results are compared with experimental measurements. Finally, the results are summarized in Sec. V.

II. COMPUTATIONAL DETAILS

A. X-ray magnetic circular dichroism

Within the one-particle approximation, the absorption coefficient $\mu_j^\lambda(\omega)$ for incident x-ray polarization λ and photon energy $\hbar\omega$ can be determined as the probability of electronic transitions from initial core states with the total angular momentum j to final unoccupied Bloch states

$$\mu_j^\lambda(\omega) = \sum_{m_j} \sum_{n\mathbf{k}} |\langle \Psi_{n\mathbf{k}} | \Pi_\lambda | \Psi_{jm_j} \rangle|^2 \delta(E_{n\mathbf{k}} - E_{jm_j} - \hbar\omega) \times \theta(E_{n\mathbf{k}} - E_F), \quad (1)$$

where Ψ_{jm_j} and E_{jm_j} are the wave function and the energy of a core state with the projection of the total angular momentum m_j ; $\Psi_{n\mathbf{k}}$ and $E_{n\mathbf{k}}$ are the wave function and the energy of a valence state in the n -th band with the wave vector \mathbf{k} ; E_F is the Fermi energy.

Π_λ is the electron-photon interaction operator in the dipole approximation

$$\Pi_\lambda = -e\alpha\mathbf{a}_\lambda, \quad (2)$$

where α are the Dirac matrices and \mathbf{a}_λ is the λ polarization unit vector of the photon vector potential, with $a_\pm = 1/\sqrt{2}(1, \pm i, 0)$, $a_\parallel = (0, 0, 1)$. Here, + and – denote, respectively, left and right circular photon polarizations with respect to the magnetization direction in the solid. Then, x-ray magnetic circular and linear dichroisms are given by $\mu_+ - \mu_-$ and $\mu_\parallel - (\mu_+ + \mu_-)/2$, respectively. More detailed expressions of the matrix elements in the electric dipole approximation may be found in Refs. [43–45]. The matrix elements due to magnetic

dipole and electric quadrupole corrections are presented in Ref. [45].

X-ray absorption spectroscopy (XAS) provides one of the methods to quantify the strength of the SO interaction in compounds. Van der Laan and Thole showed that the so-called branching ratio $\text{BR} = I_{L_3}/I_{L_2}$ ($I_{L_{2,3}}$ is the integrated intensity of isotropic XAS at the $L_{2,3}$ edges) is an important quantity associated with SOC [46]. The BR is directly related to the ground-state expectation value of the angular part of the spin-orbit coupling $\langle \mathbf{L} \cdot \mathbf{S} \rangle$ through $\text{BR} = (2+r)/(1-r)$, where $r = \langle \mathbf{L} \cdot \mathbf{S} \rangle / n_h$ and n_h is the number of holes in $5d$ states [46]. As a result, XAS provides a direct probe of SOC, which is complementary to other techniques such as the magnetic susceptibility, electron paramagnetic resonance, and Mössbauer spectroscopy (which probe SOC through the value of the Lande g-factor).

B. RIXS

In the direct RIXS process [41] the incoming photon with energy $\hbar\omega_{\mathbf{k}}$, momentum $\hbar\mathbf{k}$, and polarization ϵ excites the solid from ground state $|g\rangle$ with energy E_g to intermediate state $|I\rangle$ with energy E_I . During relaxation an outgoing photon with energy $\hbar\omega_{\mathbf{k}'}$, momentum $\hbar\mathbf{k}'$ and polarization ϵ' is emitted, and the solid is in state $|f\rangle$ with energy E_f . As a result, an excitation with energy $\hbar\omega = \hbar\omega_{\mathbf{k}} - \hbar\omega_{\mathbf{k}'}$ and momentum $\hbar\mathbf{q} = \hbar\mathbf{k} - \hbar\mathbf{k}'$ is created. Our implementation of the code for the calculation of the RIXS intensity uses Dirac four-component basis functions [47] in the perturbative approach [48]. RIXS is a second-order process, and its intensity is given by

$$I(\omega, \mathbf{k}, \mathbf{k}', \epsilon, \epsilon') \propto \sum_f \left| \sum_I \frac{\langle f | \hat{H}'_{\mathbf{k}'\epsilon'} | I \rangle \langle I | \hat{H}'_{\mathbf{k}\epsilon} | g \rangle}{E_g - E_I} \right|^2 \times \delta(E_f - E_g - \hbar\omega), \quad (3)$$

where the RIXS perturbation operator in the dipole approximation is given by the lattice sum $\hat{H}'_{\mathbf{k}\epsilon} = \sum_{\mathbf{R}} \hat{\alpha} \epsilon \exp(-i\mathbf{k}\mathbf{R})$, where α are the Dirac matrices. The sum over intermediate states $|I\rangle$ includes the contributions from different spin-split core states at the given absorption edge. The matrix elements of the RIXS process in the frame of the fully relativistic Dirac LMTO method are presented in Ref. [49].

C. Crystal structure

$\text{Ba}_4\text{Ir}_3\text{O}_{10}$ has a monoclinic structure with the space group $P2_1/a$ (No. 14). Its unit cell contains two inequivalent Ba sites, two inequivalent Ir sites, and five inequivalent O sites (Table I) [32]. The structure is built out of Ir_3O_{12} trimers, which are formed by three face sharing IrO_6 octahedra (see Fig. 1). The two Ir atoms, Ir_1 and Ir_2 , occupy the center and outer positions of the trimer,

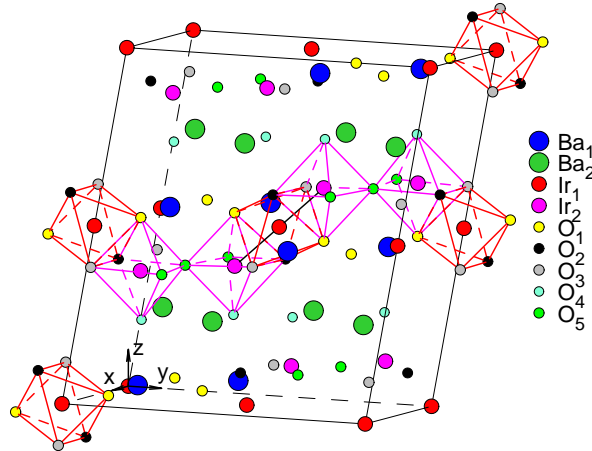


FIG. 1: (Color online) The schematic representation of $\text{Ba}_4\text{Ir}_3\text{O}_{10}$ in the monoclinic structure with the space group $P2_1/a$ (No. 14).

TABLE I: The Wyckoff positions (WP) of $\text{Ba}_4\text{Ir}_3\text{O}_{10}$ for the monoclinic $P2_1/a$ crystal structure (lattice constants $a = 5.788 \text{ \AA}$, $b = 13.222 \text{ \AA}$, $c = 7.242 \text{ \AA}$ and $\beta = 112.98^\circ$ [36]).

Structure	WP	Atom	<i>x</i>	<i>y</i>	<i>z</i>
$P2_1/a$ Ref. [36]	4e	Ba ₁	0.9695	0.6387	0.9259
	4e	Ba ₂	0.2640	0.6131	0.5198
	2a	Ir ₁	0	0	0
	4e	Ir ₂	0.1339	0.8505	0.2496
	4e	O ₁	0.0179	0.1500	0.0647
	4e	O ₂	0.6665	0.0291	0.7829
	4e	O ₃	0.1244	0.0382	0.7829
	4e	O ₄	0.7278	0.1531	0.4625
	4e	O ₅	0.5861	0.2339	0.7638

respectively. Such trimeric building blocks are connected by corners. This arrangement leads to the formation of zigzag chains of Ir_3O_{12} trimers running along the b axis.

Ir_1 and Ir_2 belong to intratrimer face-sharing and intertrimer corner-sharing octahedra, respectively. Two outside octahedra around the Ir_2 ions of each trimer are strongly distorted, chiefly due to the connection to the octahedra of adjacent trimers. The middle octahedra around the Ir_1 ions are less distorted. The corresponding $\text{Ir}_1\text{-O}_1$, $\text{Ir}_1\text{-O}_2$, and $\text{Ir}_1\text{-O}_3$ distances for the monoclinic $P2_1/a$ structure are equal to 2.0312, 1.9941, and 2.0321 \AA , respectively. The $\text{Ir}_2\text{-O}_1$, $\text{Ir}_2\text{-O}_2$, $\text{Ir}_2\text{-O}_3$, $\text{Ir}_2\text{-O}_4$, and $\text{Ir}_2\text{-O}_5$ distances are equal to 2.0956, 2.0338, 2.0448, 1.9201, and 1.9777 \AA , respectively. The shortest Ir-Ir bond is the one between Ir_1 and Ir_2 within the trimers, which has a length of 2.5849 \AA , shorter than that of the metallic iridium ($\sim 2.71 \text{ \AA}$ [34]). The average bond lengths are equal to 2.019 \AA and 2.008 \AA for the octahedra around Ir_1 and Ir_2 ions, respectively.

D. Calculation details

The details of the computational method are described in our previous papers [49–52] and here we only mention several aspects. The band structure calculations were performed using the fully relativistic LMTO method [44, 53]. This implementation of the LMTO method uses four-component basis functions constructed by solving the Dirac equation inside an atomic sphere [47]. The exchange-correlation functional of a GGA-type was used in the version of Perdew, Burke and Ernzerhof [54]. The Brillouin zone integration was performed using the improved tetrahedron method [55]. The basis consisted of Ir and Ba s , p , d , and f ; and O s , p , and d LMTO’s.

To consider the electron-electron correlation effects we used the relativistic generalization of the rotationally invariant version of the GGA+ U method [56] which considers that, in the presence of spin-orbit coupling, the occupation matrix of localized electrons becomes nondiagonal in spin indexes. Hubbard U was considered an external parameter and varied from 0.65 to 3.65 eV. We used the value of Hund’s coupling $J_H = 0.65 \text{ eV}$ obtained from constrained LSDA calculations [57, 58]. Thus, the parameter $U_{\text{eff}} = U - J_H$, which roughly determines the splitting between the lower and upper Hubbard bands, varied between 0 and 3.0 eV. We adjusted the value of U to achieve the best agreement with the experiment.

In the RIXS process, an electron is promoted from a core level to an intermediate state, leaving a core hole. As a result, the electronic structure of this state differs from that of the ground state. To reproduce the experimental spectrum, the self-consistent calculations should be carried out including the core hole. Usually, the core-hole effect has no impact on the shape of XAS at the $L_{2,3}$ edges of 5d systems and has just a minor effect on the XMCD spectra at these edges [44]. However, the core hole has a strong effect on the RIXS spectra in transition metal compounds [49, 59], and we consider it in our calculations.

Note, that in our calculations, we rely on the experimentally measured atomic positions and lattice constants, because they are well established for this material and still probably more accurate than those obtained from DFT.

III. ELECTRONIC AND MAGNETIC STRUCTURES

We performed GGA, GGA+SO, and GGA+SO+ U calculations of the electronic and magnetic structures of $\text{Ba}_4\text{Ir}_3\text{O}_{10}$ for the experimental crystal structure [36] (see Table I). The crystal field at the Ir site (Ci and $C1$ point symmetry for Ir_1 and Ir_2 sites, respectively) causes the splitting of 5d orbitals into five singlets d_{3z^2-1} , $d_{x^2-y^2}$, d_{xy} , d_{xz} , and d_{yz} . In Fig. 2 the calculated orbital-resolved t_{2g} partial density of states (DOS) for $\text{Ba}_4\text{Ir}_3\text{O}_{10}$ is presented. Both the Ir_1 and Ir_2 ions possess strong

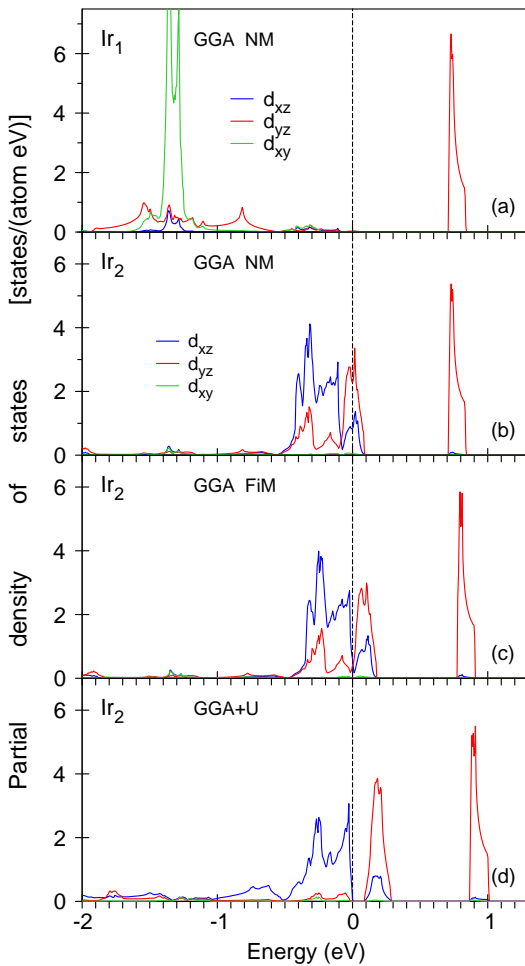


FIG. 2: (Color online) The orbital-resolved Ir t_{2g} partial density of states [in states/(atom eV)] for $\text{Ba}_4\text{Ir}_3\text{O}_{10}$ calculated in the GGA for the nonmagnetic solution at the Ir_1 site (a), and the Ir_2 site (b). The results of the ferrimagnetic (FiM) solution (c) and the GGA+ U results (d) for the Ir_2 site.

DOS peaks at ~ 0.8 eV, which indicate tetravalent Ir^{4+} states ($5d^5$). The partial DOS is quite different for two nonequivalent Ir sites.

Every Ir_1 ion has two neighboring Ir ions in its close vicinity at ~ 2.58 Å [31, 33], while Ir_2 ions have only one neighboring Ir ion at the same distance (see Fig. 1). As a result, the Ir_1 ions have a tendency of forming quasi-molecular orbital (QMO) states and dimerization. The d_{xy} , d_{yz} , and d_{xz} orbitals represent the character of the bands for the t_{2g} states at the Ir_1 site. The d_{yz} orbital, directed along the trimer bond, provides the dominant character of the two subbands stemming from t_{2g} -derived bands: the lowest (-1.5 eV) occupied subband and the highest (+0.8 eV) empty subband. The two subbands with predominant d_{yz} character can be assigned to the bonding and antibonding states of Ir_1 dimer molecules with a splitting energy of ~ 2.3 eV. In stark contrast, there are strong peaks at the Fermi level from the d_{yz}

and d_{xz} orbitals at the Ir_2 sites in the GGA approach for the nonmagnetic case [see Fig. 2(b)]. They determine a metallic solution for the ground state of $\text{Ba}_4\text{Ir}_3\text{O}_{10}$. The ferrimagnetic (FiM) solution produces a quasi-gap at the Fermi level [see Fig. 2(c)], although the system is still in a metallic state. However, electrical resistivity shows a clear insulating state across the entire temperature range measured up to 400 K [31]. For an insulating solution for the ground state of $\text{Ba}_4\text{Ir}_3\text{O}_{10}$ one has to take into account strong Coulomb correlations at the Ir_2 site. Due to relatively small DOS at the Fermi level for the FiM solution, even small Hubbard $U_{\text{eff}} \geq 0.35$ eV applied only for the Ir_2 site is able to produce an energy gap and an insulating ground state for $\text{Ba}_4\text{Ir}_3\text{O}_{10}$ [Fig. 2(d)]. Here we have quite a unique situation when the insulating state in $\text{Ba}_4\text{Ir}_3\text{O}_{10}$ is driven by both the dimerization at the Ir_1 site and Mott insulating behavior at the Ir_2 one.

The dimerization of transition-metal ions has been frequently seen, for example, in a wide variety of honeycomb-based $3d$, $4d$, and $5d$ oxides and halides, including $\alpha\text{-TiCl}_3$ [60], $\alpha\text{-MoCl}_3$ [61], Li_2RuO_3 [62], $\alpha\text{-RuCl}_3$ [63], Na_2IrO_3 [64, 65], and the high pressure $\beta\text{-Li}_2\text{IrO}_3$ iridate [6, 66, 67].

Figures 3(a) and 3(b) show the fully relativistic GGA+SO t_{2g} bands and partial DOS for Ir_1 and Ir_2 sites, respectively, presented by circles proportional in size to their orbital character projected onto the basis set of Ir $d_{3/2}$ (the relativistic quantum number $\kappa = 2$, the blue curve) and $d_{5/2}$ ($\kappa = -3$, the red curve) states. According to the partial DOS, the occupied energy bands for the Ir_1 and Ir_2 sites are well separated and lie in the energy intervals from -2 to -0.85 eV and from -0.85 eV to E_F , respectively. In the strong SOC limit, the t_{2g} band at the Ir_2 site splits into effective total angular momentum $J_{\text{eff}} = 1/2$ doublet and $J_{\text{eff}} = 3/2$ quartet bands. The functions of the $J_{\text{eff}} = 3/2$ quartet are dominated by $d_{3/2}$ states with some weight of $d_{5/2}$ ones. The $J_{\text{eff}} = 1/2$ functions are almost completely given by the linear combinations of $d_{5/2}$ states [Fig. 3(a)]. The GGA+SO+ U approach in agreement with the experiment [31] gives an insulating ground state for $\text{Ba}_3\text{InIr}_2\text{O}_9$ [Fig. 3(c)] with three narrow empty peaks just above the Fermi level. We found that the best agreement between the calculated and experimentally measured RIXS spectra at the Ir L_3 edge can be achieved for $U_{\text{eff}} = 1.3$ eV (see Section IV).

To better understanding the influence of on-site Coulomb interaction and the spin-orbit coupling in the electronic structure and the energy band formation in $\text{Ba}_4\text{Ir}_3\text{O}_{10}$ we present in Figure 4 a phase diagram in the $U_{\text{eff}}\text{-SOC}$ plane for $\text{Ba}_4\text{Ir}_3\text{O}_{10}$ in comparison with Sr_2IrO_4 [68]. To obtain this diagram we tuned the SOC term for the Ir $5d$ orbitals. A scaling factor λ in the SOC term of the Hamiltonian is introduced in the second variational step [69]. In this way, we can enhance the effect of SOC by taking $\lambda > 1$ or reduce it by taking $\lambda < 1$. For $\lambda = 0$ there is no SOC at all, while $\lambda = 1$ refers to the self-consistent reference value. The blue solid-circled and

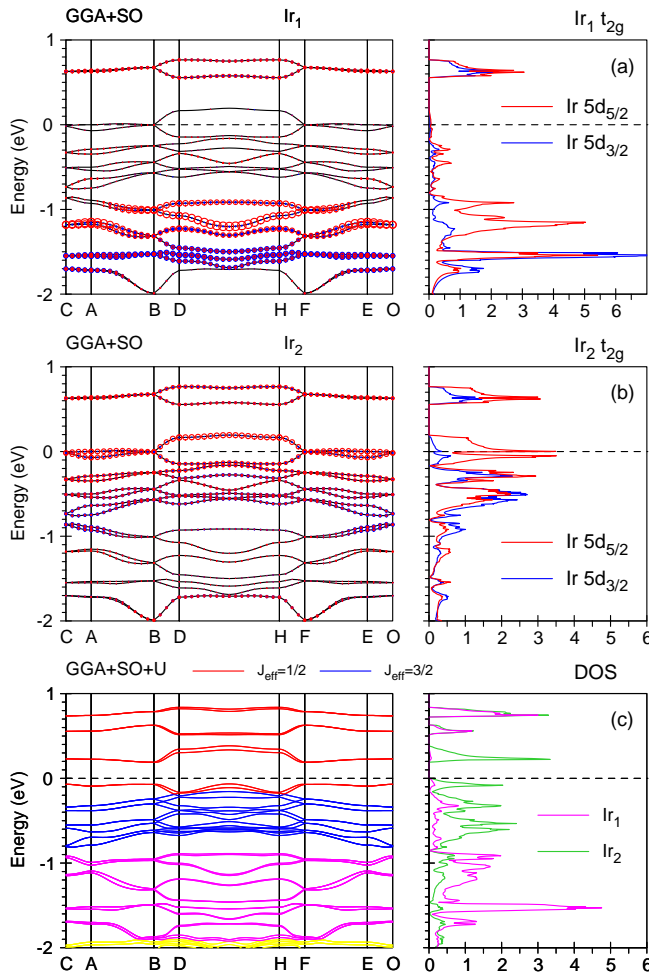


FIG. 3: (Color online) The energy band structure of $\text{Ba}_4\text{Ir}_3\text{O}_{10}$ and 5d partial density of states for Ir_1 (the upper panel) and Ir_2 (the middle panel) calculated in the fully relativistic Dirac GGA+SO approximation. The circles are proportional in size to their orbital character projected onto the basis set of Ir $d_{3/2}$ (the relativistic quantum number $\kappa = 2$, the blue curve) and $d_{5/2}$ ($\kappa = -3$, the red curve) states; (the lower panel) the energy bands calculated in the GGA+SO+ U approximation with $U_{\text{eff}} = 1.3$ eV.

red solid-circled curves in Fig. 4 separate metal (under the curves) and Mott insulator (above the curves) states connected via a first-order phase transition for $\text{Ba}_4\text{Ir}_3\text{O}_{10}$ and Sr_2IrO_4 , respectively. In the case of Sr_2IrO_4 , the energy gap opens up for $\lambda = 0$ with $U_{\text{eff}}^c = 2.1$ eV and for $\lambda = 2.2$ with $U_{\text{eff}}^c = 0$ eV, the greater the value of U_{eff} , the lower the value of λ is for the phase transition. For $\text{Ba}_4\text{Ir}_3\text{O}_{10}$ the energy gap opens up for $\lambda = 0$ with $U_{\text{eff}}^c = 0.91$ eV, and for $\lambda = 1.85$ with $U_{\text{eff}}^c = 0$ eV. We can see that $\text{Ba}_4\text{Ir}_3\text{O}_{10}$ possesses a larger $U_{\text{eff}}-\text{SOC}$ Mott-dielectric phase space in comparison with Sr_2IrO_4 .

Figures 5 and 6 present the energy band structure and partial DOS, respectively, calculated for $\text{Ba}_4\text{Ir}_3\text{O}_{10}$ in the GGA+SO+ U approach with $U_{\text{eff}} = 1.3$ eV. The occu-

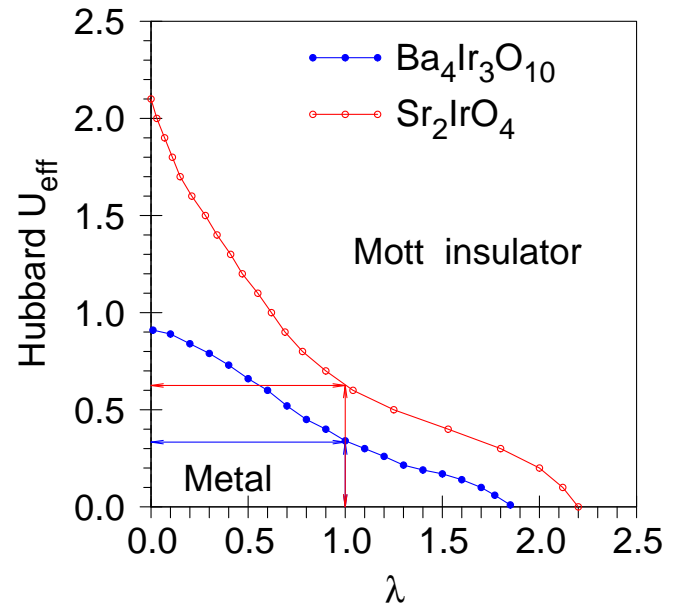


FIG. 4: (Color online) The phase diagram in the $U_{\text{eff}}-\text{SOC}$ plane for $\text{Ba}_4\text{Ir}_3\text{O}_{10}$ (the blue curve) in comparison with Sr_2IrO_4 [68] (the red curve). The curves separate metal (under the curves) and Mott insulator (above the curves) states for $\text{Ba}_4\text{Ir}_3\text{O}_{10}$ and Sr_2IrO_4 , connected via a first-order phase transition. The horizontal lines indicate the value of Hubbard U_{eff} for which the energy band gap opens up.

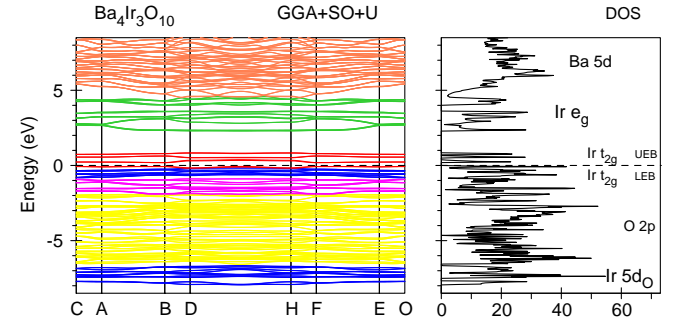


FIG. 5: (Color online) The energy band structure and total density of states (DOS) [in states/(cell eV)] for $\text{Ba}_4\text{Ir}_3\text{O}_{10}$ calculated in the GGA+SO+ U approach ($U_{\text{eff}} = 1.3$ eV).

pied t_{2g} states [the low energy band (LEB)] are situated in the energy interval from -0.85 eV to E_F . The empty t_{2g} states [the upper energy band (UEB)] consist of three narrow single peaks divided by energy gaps and occupy the energy range from 0.25 to 0.85 eV. There is a significant amount of Ir 5d DOS located at the bottom of oxygen 2p states from -7.9 to -4.5 eV below the Fermi energy. These so called Ir $5d_O$ states are provided by the tails of oxygen 2p states inside the Ir atomic spheres and play an essential role in the RIXS spectrum at the Ir L_3 edge (see Section IV).

The Ba 5d states occupy the energy region from 4.8 to

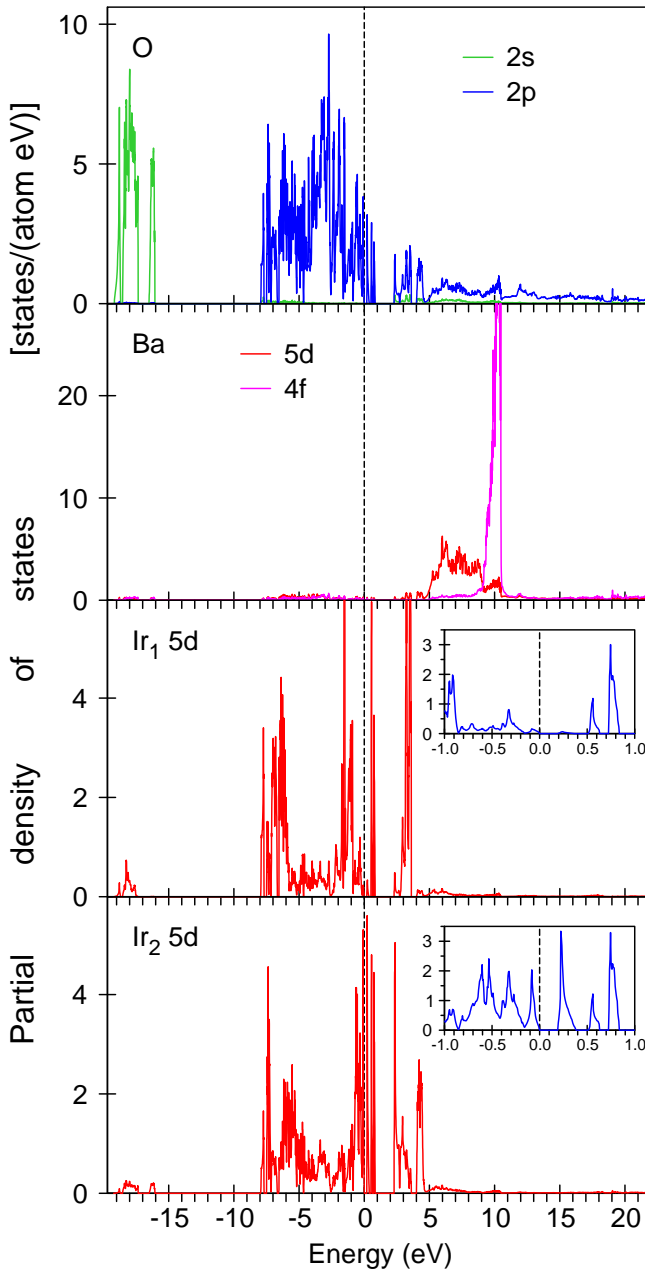


FIG. 6: (Color online) The partial density of states (DOS) [in states/(atom eV)] for $\text{Ba}_4\text{Ir}_3\text{O}_{10}$ calculated in the GGA+SO+ U approach ($U_{\text{eff}} = 1.3$ eV).

9.1 eV above the Fermi energy. A narrow and intensive DOS peak of Ba 4f states is located just above the Ba 5d states from 9.1 to 10.8 eV. The oxygen 2s states are situated far below the Fermi level from -19.3 to -16.1 eV. The occupied O 2p states are localized from -7.9 eV to E_F . They are strongly hybridized with Ir 5d states. The empty oxygen 2p states are strongly hybridized with Ir t_{2g} UEB just above the Fermi level and with the Ir e_g states. They are also hybridized with Ba 5d and 4f states.

TABLE II: The theoretically calculated in the GGA+SO+ U approach ($U_{\text{eff}} = 1.3$ eV) spin M_s , orbital M_l , and total M_{tot} magnetic moments (in μ_{B}) in $\text{Ba}_4\text{Ir}_3\text{O}_{10}$ for the FiM solution.

atom	M_s	M_l	M_{tot}
Ba_1	-0.0016	0.0003	-0.0013
Ba_2	-0.0015	0.0014	-0.0001
Ir_1	0.0590	0.0026	0.0616
Ir_2	-0.0748	-0.0471	-0.1219
O_1	0.0013	-0.0034	-0.0021
O_2	-0.0026	0.0031	0.0005
O_3	-0.0028	0.0024	-0.0004
O_4	-0.0235	-0.0208	-0.0443
O_5	-0.0103	-0.0068	-0.0171

Table II presents the theoretically calculated in the GGA+SO+ U approach ($U_{\text{eff}} = 1.3$ eV) spin M_s , orbital M_l , and total M_{tot} magnetic moments in $\text{Ba}_4\text{Ir}_3\text{O}_{10}$ for the FiM solution. The spin and orbital moments at the Ir_1 site in $\text{Ba}_4\text{Ir}_3\text{O}_{10}$ equal to 0.0590 and 0.0026 μ_{B} , respectively. They have the same direction since the Ir 5d states are more than half filled. The spin and orbital moments at the Ir_2 site equal to -0.0748 and -0.0471 μ_{B} , respectively. The ratio M_l/M_s is equal to 0.04 and 0.63 for the Ir_1 and Ir_2 sites, respectively. The corresponding ratio is equal to 1.68 in the SOC driven $J_{\text{eff}} = \frac{1}{2}$ iridate Sr_2IrO_4 [7]. It indicates a weaker coupling between the local orbital and spin moments in $\text{Ba}_4\text{Ir}_3\text{O}_{10}$ in comparison with Sr_2IrO_4 .

IV. XAS, XMCD AND RIXS SPECTRA

A. Ir $L_{2,3}$ XAS and XMCD spectra

Figure 7 presents the XAS (the upper panel) and XMCD spectra (the lower panel) at the Ir $L_{2,3}$ edges for $\text{Ba}_4\text{Ir}_3\text{O}_{10}$ calculated in the GGA+SO+ U ($U_{\text{eff}} = 1.3$ eV) approach. The isotropic XAS spectra are dominated by empty e_g states with a smaller contribution from empty t_{2g} orbitals at lower energy. The XMCD spectra, however, mainly come from the t_{2g} orbitals. This results in a shift between the maxima of the XAS and XMCD spectra.

In the limit of negligible SOC effects, the statistical branching ratio $\text{BR} = I_{L_3}/I_{L_2} = 2$, and the L_3 white line is twice the size of the L_2 feature [46]. The theoretically calculated BR in $\text{Ba}_4\text{Ir}_3\text{O}_{10}$ is 2.45 for the Ir_1 site and 3.13 for the Ir_2 site. The theoretically calculated BR for Sr_2IrO_4 with strong SOC is equal to 3.56 [68]. Relatively moderate SOC together with molecular orbital-like states at the Ir_1 site in $\text{Ba}_4\text{Ir}_3\text{O}_{10}$ suggest that the strongly spin-orbit coupled pure $J_{\text{eff}} = 1/2$ picture is not appropriate for the Ir_1 site. It is better use a description based on molecular orbital-like states. However, the $J_{\text{eff}} = 1/2$ model is still valid for the Ir_2 site (see Fig. 3).

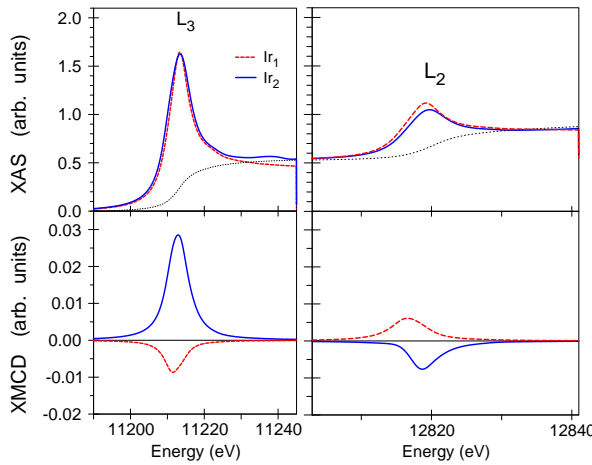


FIG. 7: (Color online) The theoretically calculated x-ray absorption (the upper panels) and XMCD spectra (the lower panels) at the Ir $L_{2,3}$ edges in $\text{Ba}_4\text{Ir}_3\text{O}_{10}$ for the monoclinic $P2_1/a$ crystal structure in the GGA+SO+ U approach ($U_{\text{eff}} = 1.3$ eV). The dotted black curves in the upper panels show the background scattering intensity.

B. Ir RIXS spectra

The experimental RIXS spectrum at the Ir L_3 edge was measured by Shen *et al.* [40] in the energy range up to 5 eV. In addition to the elastic peak centered at zero energy loss, the spectrum consists of several peaks below 2.3 eV and a strong peak at 3.7 eV. We found that the fine structure situated below 2.3 eV corresponds to intra- t_{2g} excitations. These peaks are very sensitive to the value of the energy gap in $\text{Ba}_4\text{Ir}_3\text{O}_{10}$ and the relative position of t_{2g} LEB and UEB (Fig. 5). Figure 8 shows the experimental RIXS spectrum measured by Shen *et al.* [40] compared with the theoretical spectra calculated for $t_{2g} \rightarrow t_{2g}$ transitions in the GGA+SO and GGA+SO+ U approaches for the FiM solution for different U_{eff} values. The best agreement was found for $U_{\text{eff}} = 1.3$ eV. The GGA+SO calculations as well as the GGA+SO+ U approach with smaller U_{eff} do not produce adequate agreement with the experimental data. The larger values of U_{eff} shift the RIXS spectrum towards higher energies.

There is a low energy peak at ~ 0.1 eV which is not produced by our first-principle RIXS calculations. Shen *et al.* [40] show that this peak belongs to low-energy magnetic excitations. It is interesting to note that the reference iridate Sr_2IrO_4 also possesses a low energy peak at 0.1 eV, which is considered in Ref. [70] as magnon excitations in agreement with scanning tunneling microscope measurements [71]. The theoretical description of magnon and exciton spectra demands a many-body approach beyond the one-particle approximation, such as the Bethe-Salpiter equation for exciton spectra and calculations of the magnon dispersion and the electron-magnon interaction for magnon spectra.

Figure 9(a) presents the theoretically calculated and

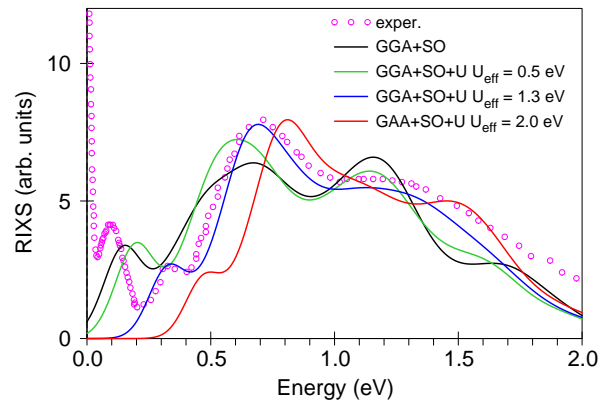


FIG. 8: (Color online) The experimental resonance inelastic x-ray scattering spectrum (open magenta circles) measured by Shen *et al.* [40] at the Ir L_3 edge in $\text{Ba}_4\text{Ir}_3\text{O}_{10}$ compared with the theoretically calculated ones for different approaches.

experimentally measured RIXS spectra at the Ir L_3 edge for $\text{Ba}_4\text{Ir}_3\text{O}_{10}$ [40] in a wide energy interval up to 12 eV. Figure 9(b) shows the partial contributions from different transitions between the energy bands presented in Fig. 5 in comparison with the experimental spectrum [40]. As we mentioned above, the peaks situated below 2.3 eV correspond to intra- t_{2g} excitations (the blue curve in Fig. 9). The peak located at ~ 3.7 eV was found to be due to $t_{2g} \rightarrow e_g$ transitions (the red curve). The $\text{O}_{2p} \rightarrow t_{2g}$ transitions (the black curve) also contribute to this peak. There are three peaks above 5 eV which can be associated with $\text{O}_{2p} \rightarrow t_{2g}$ (the black curve) and $\text{O}_{2p} \rightarrow e_g$ (the magenta curve) transitions, as well as charge-transfer excitations $5d_{\text{O}} \rightarrow t_{2g}$ (the green curve) and $5d_{\text{O}} \rightarrow e_g$ (the blue dashed curve). The theoretical calculations are in good agreement with the experimental data.

Figure 10 shows the theoretically calculated in the GGA+SO+ U approach RIXS spectrum at the O K edge in $\text{Ba}_4\text{Ir}_3\text{O}_{10}$. The fine structures at ≤ 2.3 eV are derived from the interband transitions between the oxygen $2p$ states strongly hybridized with the Ir t_{2g} states in close vicinity to the Fermi level: the $\text{O}_{t_{2g}} \rightarrow \text{O}_{t_{2g}}$ transitions (the blue curve). However, the $\text{O}_{t_{2g}} \rightarrow \text{O}_{e_g}$ transitions are very weak (the black curve). The major two-peak fine structure situated at 2–7 eV is quite intensive and derived from the $\text{O}_{2p} \rightarrow \text{O}_{t_{2g}}$ transitions (the red curve). The $\text{O}_{2p} \rightarrow \text{O}_{e_g}$ transitions are less intensive (the magenta curve). The narrow peak at 7–9 eV is due to $5d_{\text{O}} \rightarrow \text{O}_{t_{2g}}$ transitions (the blue dashed curve). Experimental measurements of the RIXS spectrum at the O K edge in $\text{Ba}_4\text{Ir}_3\text{O}_{10}$ are highly desirable.

V. CONCLUSIONS

To summarize, we have investigated the electronic structure of $\text{Ba}_4\text{Ir}_3\text{O}_{10}$ in the frame of the fully rela-

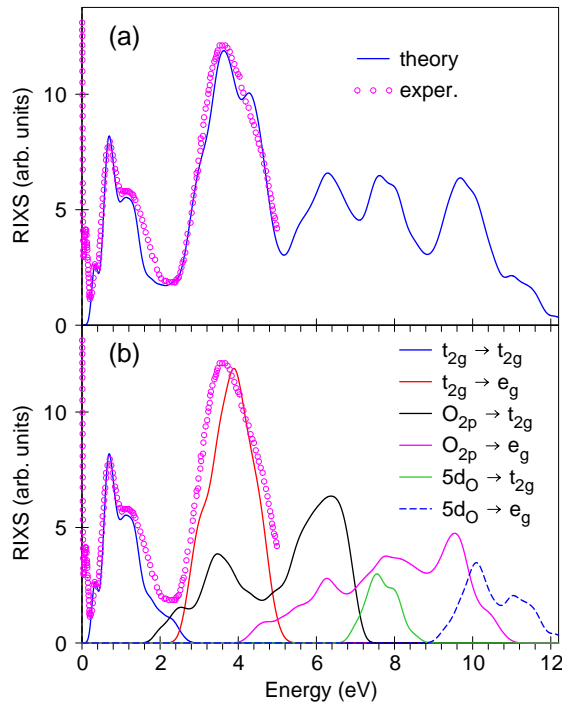


FIG. 9: (Color online) (a) The experimental resonance inelastic x-ray scattering spectrum (open magenta circles) measured by Shen *et al.* [40] at the Ir L_3 edge in $\text{Ba}_4\text{Ir}_3\text{O}_{10}$ compared with the theoretically calculated one in the GGA+SO+ U approach ($U_{\text{eff}} = 1.3$ eV); (b) partial contributions from different transitions between the energy bands presented in Fig. 5 in comparison with the experimental spectrum [40].

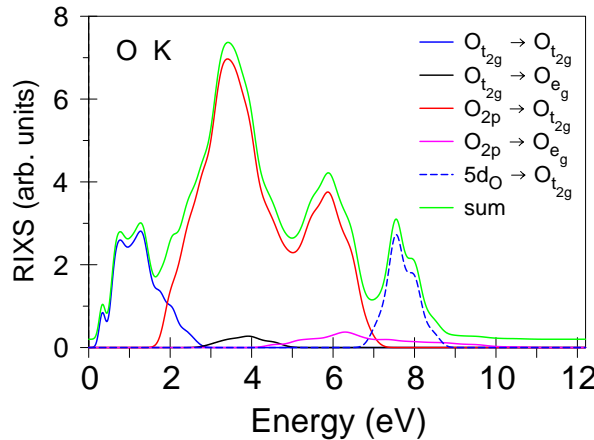


FIG. 10: (Color online) Partial contributions from different transitions between the energy bands at the O K edge in $\text{Ba}_4\text{Ir}_3\text{O}_{10}$ calculated in the GGA+SO+ U approach ($U_{\text{eff}} = 1.3$ eV).

tivistic spin-polarized Dirac approach. We have also presented comprehensive theoretical calculations of the RIXS spectra at the Ir L_3 and oxygen K edges, as well as the XAS and XMCD spectra at the Ir $L_{2,3}$ edges.

The delicate interplay between electronic correlations, SOC, intersite hopping, and a crystal field splitting leads to a strongly competing ground state of $\text{Ba}_4\text{Ir}_3\text{O}_{10}$. We found that the ground magnetic state of $\text{Ba}_4\text{Ir}_3\text{O}_{10}$ is ferrimagnetic. The GGA and GGA+SO approaches give a metallic ground state in $\text{Ba}_4\text{Ir}_3\text{O}_{10}$. It is in contradiction with electric conductivity and energy loss measurements, which firmly indicate an insulating character of $\text{Ba}_4\text{Ir}_3\text{O}_{10}$. A quasi-2D structure of $\text{Ba}_4\text{Ir}_3\text{O}_{10}$ is composed of buckled sheets, which constitute corner-connected Ir_3O_{12} trimers containing three distorted face-sharing IrO_6 octahedra. The Ir atoms are distributed over two symmetrically inequivalent sites: the center of the trimer (Ir_1) and its two tips (Ir_2). The $\text{Ir}_1 - \text{Ir}_2$ distance within the trimer is quite small and equals to 2.58 Å at low temperature. As a result, the clear formation of bonding and antibonding states at the Ir_1 site occurs. The large bonding-antibonding splitting stabilizes the d_{yz} -orbital-dominant antibonding state of t_{2g} holes and produces a wide energy gap at the Fermi level. However, the energy gap opens up in $\text{Ba}_4\text{Ir}_3\text{O}_{10}$ only with taking into account strong Coulomb correlations at the Ir_2 site. Therefore, we have quite a unique situation when the insulating state in $\text{Ba}_4\text{Ir}_3\text{O}_{10}$ is driven by both the dimerization at the Ir_1 site and Mott insulating behavior at the Ir_2 one.

The theoretically calculated Ir L_3 RIXS spectrum is in good agreement with the experiment. We found that the low energy part of the RIXS spectrum ≤ 2.3 eV corresponds to intra- t_{2g} excitations. The peak located at ~ 3.7 eV was found to be due to $t_{2g} \rightarrow e_g$ transitions. The $O_{2p} \rightarrow t_{2g}$ transitions also contribute to this peak. There are three peaks above 5 eV which can be associated with $O_{2p} \rightarrow t_{2g}$ and $O_{2p} \rightarrow e_g$ transitions, as well as charge-transfer excitations $5d_O \rightarrow t_{2g}$ and $5d_O \rightarrow e_g$.

The major contribution into the RIXS spectrum at the O K edge between 2 and 7 eV comes from the $O_{2p} \rightarrow O_{t_{2g}}$ transitions. The $O_{2p} \rightarrow O_{e_g}$ transitions are less intensive. We found that the $O_{t_{2g}} \rightarrow O_{t_{2g}}$ transitions are situated below 2.3 eV, and the $O_{t_{2g}} \rightarrow O_{e_g}$ transitions are very weak. The narrow peak at 7–9 eV is due to $5d_O \rightarrow O_{t_{2g}}$ transitions.

Acknowledgments

The studies were supported by the National Academy of Sciences of Ukraine within the budget program KP-KBK 6541230 "Support for the development of priority areas of scientific research".

[1] W. Witczak-Krempa, G. Chen, Y. B. Kim, and L. Balents, Correlated quantum phenomena in the strong spin-

orbit regime, *Annu. Rev. Condens. Matter Phys.* **5**, 57

(2014).

[2] G. Jackeli and G. Khaliullin, Mott insulators in the strong spin-orbit coupling limit: From heisenberg to a quantum compass and kitaev models, *Phys. Rev. Lett.* **102**, 017205 (2009).

[3] G. Chen, R. Pereira, and L. Balents, Exotic phases induced by strong spin-orbit coupling in ordered double perovskites, *Phys. Rev. B* **82**, 174440 (2010).

[4] B. J. Kim, H. Jin, S. J. Moon, J.-Y. Kim, B.-G. Park, C. S. Leem, J. Yu, T. W. Noh, C. Kim, S.-J. Oh, J.-H. Park, V. Durairaj, G. Cao, and E. Rotenberg, Novel $j_{eff}=1/2$ mott state induced by relativistic spin-orbit coupling in Sr_2IrO_4 , *Phys. Rev. Lett.* **101**, 076402 (2008).

[5] C. Martins, M. Aichhorn, L. Vaugier, and S. Biermann, Reduced effective spin-orbital degeneracy and spin-orbital ordering in paramagnetic transition-metal oxides: Sr_2IrO_4 versus Sr_2RhO_4 , *Phys. Rev. Lett.* **107**, 266404 (2011).

[6] V. N. Antonov, S. Uba, and L. Uba, Electronic structure and x-ray magnetic circular dichroism in the hyperhoneycomb iridate beta- Li_2IrO_3 , *Phys. Rev. B* **98**, 245113 (2018).

[7] V. N. Antonov, D. A. Kukusta, and L. V. Bekenov, Electronic structure and resonant inelastic x-ray scattering of the $j_{eff} = 1/2$ mott insulator Sr_2IrO_4 from the density functional theory, *Phys. Rev. B* **109**, 165120 (2024).

[8] X.-L. Qi and S.-C. Zhang, The quantum spin hall effect and topological insulators, *Physics Today* **63**, 33 (2010).

[9] Y. Ando, Topological insulator, *J. Phys. Soc. Jpn.* **82**, 102001 (2013).

[10] T. O. Wehling, A. Black-Schafferc, and A. Balatsky, Dirac materials, *Adv. Phys.* **63**, 1 (2014).

[11] A. Bansil, L. H, and T. Das, Colloquium: Topological band theory, *Rev. Mod. Phys.* **88**, 021004 (2016).

[12] B. J. Kim, H. Ohsumi, T. Komesu, S. Sakai, T. Morita, H. Takagi, and T. Arima, Phase-sensitive observation of a spin-orbital mott state in Sr_2IrO_4 , *Science* **323**, 1329 (2009).

[13] H. Watanabe, T. Shirakawa, and S. Yunoki, Microscopic study of a spin-orbit-induced mott insulator in Ir oxides, *Phys. Rev. Lett.* **105**, 216410 (2010).

[14] W. Witczak-Krempa and Y. B. Kim, Topological and magnetic phases of interacting electrons in the pyrochlore iridates, *Phys. Rev. B* **85**, 045124 (2012).

[15] A. Go, W. Witczak-Krempa, G. S. Jeon, K. Park, and Y. B. Kim, Correlation effects on 3d topological phases: From bulk to boundary, *Phys. Rev. Lett.* **109**, 066401 (2012).

[16] A. B. Sushkov, J. B. Hofmann, G. S. Jenkins, J. Ishikawa, S. Nakatsuji, S. DasSarma, and H. D. Drew, Optical evidence for a weyl semimetal state in pyrochlore $\text{Eu}_2\text{Ir}_2\text{O}_7$, *Phys. Rev. B* **92**, 241108 (2015).

[17] I. Kimchi, J. G. Analytis, and A. Vishwanath, Three-dimensional quantum spin liquids in models of harmonic-honeycomb iridates and phase diagram in an infinite-d approximation, *Phys. Rev. B* **90**, 205126 (2014).

[18] L. Balents, Spin liquids in frustrated magnets, *Nature* **464**, 199 (2010).

[19] L. Savary and L. Balents, Quantum spin liquids: a review, *Rep. Progr. Phys.* **80**, 016502 (2017).

[20] D. I. Khomskii, *Transition Metal Compounds* (Cambridge University Press, Cambridge, 2014).

[21] K. I. Kugel, D. I. Khomskii, A. O. Sboychakov, and S. V. Streltsov, Spin-orbital interaction for face-sharing octahedra: Realization of a highly symmetric $su(4)$ model, *Phys. Rev. B* **91**, 155125 (2015).

[22] T. Sakamoto, Y. Doi, and Y. Hinatsu, Crystal structures and magnetic properties of 6H-perovskite-type oxides $\text{Ba}_3\text{MIr}_2\text{O}_9$ ($\text{M}=\text{Mg, Ca, Sc, Ti, Zn, Sr, Zr, Xd and In}$), *J. Solid State Chem.* **179**, 2995 (2006).

[23] Y. Doi and Y. Hinatsu, The structural and magnetic characterization of 6H-perovskite-type oxides $\text{Ba}_3\text{LnIr}_2\text{O}_9$ ($\text{Ln} = \text{Y, lanthanides}$), *J. Phys.: Condens. Matter* **16**, 2849 (2004).

[24] Y. Doi, K. Matsuhira, and Y. Hinatsu, Crystal structures and magnetic properties of 6H-perovskites $\text{Ba}_3\text{MRu}_2\text{O}_9$ ($\text{M} = \text{Y, In, La, Sm, Eu, and Lu}$), *J. Solid State Chem.* **165**, 317 (2002).

[25] A. Nag and S. Ray, Misjudging frustrations in spin liquids from oversimplified use of curie-weiss law, *J. Magn. Magn. Mater.* **424**, 93 (2017).

[26] D. Ziat, A. A. Aczel, R. Sinclair, Q. Chen, H. D. Zhou, T. J. Williams, M. B. Stone, A. Verrier, and J. A. Quilliam, Frustrated spin-1/2 molecular magnetism in the mixed-valence antiferromagnets $\text{Ba}_3\text{MRu}_2\text{O}_9$ ($\text{M} = \text{In, Y, Lu}$), *Phys. Rev. B* **95**, 184424 (2017).

[27] T. Dey, M. Majumder, J. C. Orain, A. Senyshyn, M. Prinz-Zwick, S. Bachus, Y. Tokiwa, F. Bert, P. Khuntia, N. Büttgen, A. A. Tsirlin, and P. Gegenwart, Persistent low-temperature spin dynamics in the mixed-valence iridate $\text{Ba}_3\text{InIr}_2\text{O}_9$, *Phys. Rev. B* **96**, 174411 (2017).

[28] J. Terzic, J. C. Wang, F. Ye, W. H. Song, S. J. Yuan, S. Aswartham, L. E. DeLong, S. V. Streltsov, D. I. Khomskii, and G. Cao, Coexisting charge and magnetic orders in the dimer-chain iridate $\text{Ba}_5\text{AlIr}_2\text{O}_11$, *Phys. Rev. B* **91**, 235147 (2015).

[29] G. Cao, J. Crow, R. Guertin, P. Henning, C. Homes, M. Strongin, D. Basov, and E. Lochner, Charge density wave formation accompanying ferromagnetic ordering in quasi-one-dimensional BaIrO_3 , *Solid State Commun.* **113**, 657 (2000).

[30] L. T. Nguyen and R. J. Cava, Trimer-based spin liquid candidate $\text{Ba}_4\text{NbIr}_3\text{O}_12$, *Phys. Rev. Materials* **3**, 014412 (2019).

[31] G. Cao, H. Zheng, H. Zhao, Y. Ni, C. A. Pocs, Y. Zhang, F. Ye, C. Hoffmann, X. Wang, M. Lee, M. Hermele, and I. Kimchi, Quantum liquid from strange frustration in the trimer magnet $\text{Ba}_4\text{Ir}_3\text{O}_10$, *npj Quantum Mater.* **5**, 26 (2020).

[32] X. Chen, Y. He, S. Wu, Y. Song, D. Yuan, E. Bourret-Courchesne, J. P. C. Ruff, Z. Islam, A. Fran, and R. J. Birgeneau, Structural and magnetic transitions in the planar antiferromagnet $\text{Ba}_4\text{Ir}_3\text{O}_10$, *Phys. Rev. B* **103**, 224420 (2021).

[33] K. E. Stitzer, M. D. Smith, and H.-C. zur Loyer, Crystal growth, structure determination and magnetic properties of $\text{Ba}_4\text{Ir}_3\text{O}_10$ and $\text{Ba}_4(\text{Co}_0.4\text{Ir}_0.6)\text{Ir}_2\text{O}_10$, *J. Appl. Crystallogr.* **338**, 104 (2002).

[34] R. W. Wyckoff, *Crystal Structures* (Wiley, New York, 1963).

[35] H. k. Müller-Buschbaum and C. Lang, $\text{Ba}_5\text{AlIr}_2\text{O}_11$: Eine neue verbindung mit iridium(iv, v), *Z. Anorg. Allg. Chem.* **568**, 29 (1989).

[36] J. Wilkens and H. Müller-Buschbaum, Zur kentttnis von $\text{Ba}_4\text{Ir}_3\text{O}_10$, *J. Inorg. Gen. Chem.* **592**, 79 (1991).

[37] Y. Klein, G. Rousse, F. Damay, F. Porcher, G. Andre, and I. Terasaki, Antiferromagnetic order and conse-

quences on the transport properties of Ba₄Ru₃O₁₀, Phys. Rev. B **84**, 054439 (2011).

[38] S. V. Streltsov and D. I. Khomskii, Unconventional magnetism as a consequence of the charge disproportionation and the molecular orbital formation in Ba₄Ru₃O₁₀, Phys. Rev. B **86**, 064429 (2012).

[39] G. Cao, H. Zhao, B. Hu, N. Pellatz, D. Reznik, P. Schlottmann, and I. Kimchi, Quest for quantum states via field-altering technology, npj Quantum Mater. **5**, 83 (2020).

[40] Y. Shen, J. Sears, G. Fabbris, A. Weichselbaum, W. Yin, H. Zhao, D. G. Mazzone, H. Miao, M. H. Upton, D. Casa, R. Acevedo-Esteves, C. Nelson, A. M. Barbour, C. Mazzoli, G. Cao, and M. P. M. Dean, Emergence of spinons in layered trimer iridate Ba₄Ir₃O₁₀, Phys. Rev. Lett. **129**, 207201 (2022).

[41] L. J. P. Ament, M. van Veenendaal, T. P. Devereaux, J. P. Hill, and J. van den Brink, Resonant inelastic x-ray scattering studies of elementary excitations, Rev. Mod. Phys. **83**, 705 (2011).

[42] F. M. F. de Groot, M. W. Haverkort, H. Elnaggar, A. Juhin, K.-J. Zhou, and P. Glatzel, Resonant inelastic x-ray scattering, Nat. Rev. Methods Primers **4**, 46 (2024).

[43] G. Y. Guo, H. Ebert, W. M. Temmerman, and P. J. Durham, First-principles calculation of magnetic circular x-ray dichroism in Fe and Co multilayers, Phys. Rev. B **50**, 3861 (1994).

[44] V. Antonov, B. Harmon, and A. Yaresko, *Electronic Structure and Magneto-Optical Properties of Solids* (Kluwer, Dordrecht, 2004).

[45] E. Arola, M. Horne, P. Strange, H. Winter, Z. Szotek, and W. M. Temmerman, Self-interaction-corrected relativistic theory of magnetic scattering of x rays: Application to praseodymium, Phys. Rev. B **70**, 235127 (2004).

[46] G. van der Laan and B. T. Thole, Local probe for spin-orbit interaction, Phys. Rev. Lett. **60**, 1977 (1988).

[47] V. V. Nemoshkalenko, A. E. Krasovskii, V. N. Antonov, V. N. Antonov, U. Fleck, H. Wonn, and P. Ziesche, The relativistic linear muffin-tin orbital method. application to Au, Phys. status solidi B **120**, 283 (1983).

[48] E. Arola, P. Strange, and B. L. Gyorffy, Relativistic theory of magnetic scattering of x rays: Application to ferromagnetic iron, Phys. Rev. B **55**, 472 (1997).

[49] V. N. Antonov, D. A. Kukusta, and L. V. Bekenov, Electronic structure and resonant inelastic x-ray scattering in the osmates: I. perovskite NaOsO₃, Phys. Rev. B **105**, 155144 (2022).

[50] V. N. Antonov, O. Jepsen, A. N. Yaresko, and A. P. Shpak, Electronic structure and x-ray magnetic circular dichroism in the heusler alloy Co₂MnGe, J. Appl. Phys. **100**, 043711 (2006).

[51] V. N. Antonov, B. N. Harmon, A. N. Yaresko, and A. P. Shpak, X-ray magnetic circular dichroism in the GdN: First-principles calculations, Phys. Rev. B **75**, 184422 (2007).

[52] V. N. Antonov, A. N. Yaresko, and O. Jepsen, X-ray magnetic dichroism in the III–V diluted magnetic semiconductors: First principle calculations, Phys. Rev. B **81**, 075209 (2010).

[53] O. K. Andersen, Linear methods in band theory, Phys. Rev. B **12**, 3060 (1975).

[54] J. P. Perdew, K. Burke, and M. Ernzerhof, Generalized gradient approximation made simple, Phys. Rev. Lett. **77**, 3865 (1996).

[55] P. E. Blöchl, O. Jepsen, and O. K. Andersen, Improved tetrahedron method for brilleyin-zane integrations, Phys. Rev. B **49**, 16223 (1994).

[56] A. N. Yaresko, V. N. Antonov, and P. Fulde, Localized u 5f electrons in UPd₃ from LDA+U calculations, Phys. Rev. B **67**, 155103 (2003).

[57] P. H. Dederichs, S. Blügel, R. Zeller, and H. Akai, Ground states of constrained systems: application to cerium impurities, Phys. Rev. Lett. **53**, 2512 (1984).

[58] W. E. Pickett, S. C. Erwin, and E. C. Ethridge, Reformulation of the LDA+U method for a local-orbital basis, Phys. Rev. B **58**, 1201 (1998).

[59] V. N. Antonov, D. A. Kukusta, and L. V. Bekenov, Electronic structure and resonant inelastic x-ray scattering in the osmates: II. pyrochlore Cd₂Os₂O₇, Phys. Rev. B **105**, 155145 (2022).

[60] S. Ogawa, Magnetic transition in TiCl₃, J. Phys. Soc. Jpn. **15**, 1901 (1960).

[61] M. A. McGuire, J. Yan, P. Lampen-Kelley, A. F. May, V. R. Cooper, L. Lindsay, A. Puretzky, L. Liang, S. KC, E. Cakmak, S. Calder, and B. C. Sales, High temperature magneto-structural transition in van der Waals-layered-MoCl₃, Phys. Rev. Mater. **1**, 064001 (2017).

[62] Y. Miura, Y. Yasui, M. Sato, N. Igawa, and K. Kakurai, New-type phase transition of Li₂RuO₃ with honeycomb structure, J. Phys. Soc. Jpn. **76**, 033705 (2007).

[63] S. Agrestini, C.-Y. Kuo, K.-T. Ko, Z. Hu, D. Kasinathan, H. B. Vasili, J. Herrero-Martin, S. M. Valvidares, E. Pellegrin, L.-Y. Jang, A. Henschel, M. Schmidt, A. Tanaka, and L. H. Tjeng, Electronically highly cubic conditions for Ru in alpha-RuCl₃, Phys. Rev. B **96**, 161107(R) (2017).

[64] I. I. Mazin, H. O. Jeschke, K. Foyevtsova, R. Valenti, and D. I. Khomskii, Na₂IrO₃ as a molecular orbital crystal, Phys. Rev. Lett. **109**, 197201 (2012).

[65] K. Foyevtsova, H. O. Jeschke, I. I. Mazin, D. I. Khomskii, and R. Valenti, Ab initio analysis of the tight-binding parameters and magnetic interactions in Na₂IrO₃, Phys. Rev. B **88**, 035107 (2013).

[66] T. Takayama, A. Krajewska, A. S. Gibbs, A. N. Yaresko, H. Ishii, H. Yamaoka, K. Ishii, N. Hiraoka, N. P. Funnell, C. L. Bull, and H. Takagi, Phys. Rev. B **99**, 125127 (2019).

[67] V. N. Antonov, D. A. Kukusta, L. Uba, A. Bonda, and S. Uba, Resonant inelastic x-ray scattering spectra in the hyperhoneycomb iridate beta-Li₂IrO₃: First-principles calculations, Phys. Rev. B **103**, 235127 (2021).

[68] V. N. Antonov, D. A. Kukusta, and L. V. Bekenov, Electronic structure and resonant inelastic x-ray scattering in the mixed 3d-5d transition-metal oxides Sr₃CuIrO₆, Sr₃CuPtO₆, and Sr₃ZnIrO₆, J. Electron. Spectrosc. Relat. Phenom. **270**, 147416 (2024).

[69] D. D. Koelling and B. N. Harmon, A technique for relativistic spin-polarised calculations, J. Phys. C **10**, 3107 (1977).

[70] J. Kim, M. Daghofer, A. H. Said, T. Gog, J. van den Brink, G. Khaliullin, and B. J. Kim, Excitonic quasiparticles in a spin-orbit mott insulator, Nature Comm. **5**, 4453 (2014).

[71] J. Nichols, N. Bray-Ali, A. Ansary, G. Cao, and K.-W. Ng, Tunneling into the mott insulator Sr₂IrO₄, Phys. Rev. B **89**, 085125 (2014).